Article Volume 15, Issue 6, 2025, 86 https://doi.org/10.33263/BRIAC156.086

Reduction of Ciprofloxacin Concentration in Wastewater Treatment Plant Effluent Using nZVI-MXene

Intania Ika Fairuzi ¹, Adhi Yuniarto ^{1,*}, Ervin Nurhayati ¹, Alfan Purnomo ¹

- Department of Environmental Engineering, Faculty of Civil, Planning and Geo Engineering, Institut Teknologi Sepuluh Nopember, Kampus ITS Sukolilo, Surabaya 60112, Indonesia; intaniaikafairuzi@gmail.com (I.I.F.); adhy@its.ac.id (A.Y.); ervin@its.ac.id (E.N.); alfan_p@its.ac.id (A.P.);
- * Correspondence: adhy@its.ac.id;

Received: 11.03.2025; Accepted: 10.05.2025; Published: 14.11.2025

Abstract: Ciprofloxacin (CPFX) is the most widely used antibiotic, and it ranges from 31-50 mg/L in WWTP. Nano zero valent iron (nZVI) has advantages in terms of reducibility and reactivity. However, the effectiveness of nZVI reduction will increase if the nanoparticles are coated. Mxene (Ti₃C₂T_x) is a two-dimensional layered material that facilitates high-speed electron transport. This material can be used as a coating material for nZVI to increase efficiency. CPFX reduction was then carried out at specific concentrations using nZVI, MXene, and nZVI/MXene nanocomposites. Each nanocomposite was characterized using SEM, EDX, BET, and FTIR analysis to determine its morphology, distribution, and chemical bonds. In this study, the efficiency of nZVI-MXene in removing CPFX solution was optimal at a concentration of 100 mg/L, with a removal efficiency of 94%. When the CPFX concentration exceeds 100 mg/L, the material removal efficiency will decrease to 11%. nZVI, MXene, and mZVI-MXene materials have an optimum contact time of 30 minutes. These findings indicate that nZVI-MXene nanocomposites at a 2:1 ratio can effectively reduce CPFX and exhibit advantages over previously studied materials. However, further treatment, such as photocatalytic processes, is needed to ensure the remaining CPFX is safe for the aquatic ecosystem.

Keywords: ciprofloxacin; nanoparticles; nZVI, Ti₃C₂T_x; WWTP.

© 2025 by the authors. This article is an open-access article distributed under the terms and conditions of the Creative Commons Attribution (CC BY) license (https://creativecommons.org/licenses/by/4.0/), which permits unrestricted use, distribution, and reproduction in any medium, provided the original work is properly cited. The authors retain copyright of their work, and no permission is required from the authors or the publisher to reuse or distribute this article, as long as proper attribution is given to the original source.

1. Introduction

Pharmaceutical waste has spread and increased in aquatic environments, becoming a growing concern in recent years [1]. Pharmaceutical waste exhibits reactive, toxic, corrosive, and flammable properties, which have a significant impact on the environment and human health [2]. Pharmaceutical waste contains several drugs, such as ciprofloxacin, paracetamol, metformin, norfluoxetine, and others [3]. Ciprofloxacin (CPFX) is the most widely used antibiotic for various bacterial diseases in humans and animals [4]. The chemical structure of CPFX (C₁₇H₁₈FN₃O₃) shows a carboxylic acid functional group that can form bonds with ion exchangers [5,6]. This antibiotic is a hazardous pollutant that poses a threat to humans and ecosystems, as its accumulation in water bodies can lead to chronic diseases [7]. The CPFX in hospital outlet wastewater and from the pharmaceutical industry has a significant concentration [8]. A study on the trial of CPFX content exposure to Daphnia magna for 48 hours showed that the concentration of CPFX in the range of 0.01-100 mg/L has a toxic effect on organisms [9]. Based on previous studies, the CPFX content detected in pharmaceutical wastewater ranges

from 31-50 mg/L [10]. Meanwhile, in studies of surface water flow samples, CPFX concentrations range from 2.5-6.5 mg/L. Research on CPFX Content in Wastewater Treatment Plants (WWTP) in several countries, such as the United States, South Korea, and Pakistan, ranges from 1.3-341 μ g/L, while in Portugal, hospital waste was detected at 38.6 μ g/L [11]. Therefore, it is necessary to treat liquid waste containing CPFX so that it does not harm living things and the surrounding environment [12]. The recapitulation of CPFX concentration from different studies is shown in Table 1.

Concentration of CPFX Research on References 0.01-100 mg/L toxic effect on Daphnia magna for 48 hours [9] [10] 31-50 mg/L Pharmaceutical wastewater 2.5-6.5 mg/L Surface water flow samples [11]WWTP in the United States, South Korea, and Pakistan $1.3-341 \, \mu g/L$ [11] $38.6 \,\mu g/L$ Hospital waste in Portugal [12]

Table 1. CPFX concentration from different studies.

Various attempts have been made to reduce the concentration of CPFX [13-15]. They used some nanoparticles and their modifications to reduce this antibiotic[16-19]. Nano Zero Valent Iron (nZVI) has the advantages of small particle size, strong reducibility, good reactivity, and magnetic separation [20]. Previous studies have shown that nZVI nanocomposites can effectively reduce the content of antibiotics and dyes in water bodies [21,22]. MXene ($T_{13}C_{2}T_{x}$) is a new two-dimensional layered material that is currently developing rapidly and is known for its anti-corrosion and anti-wear properties [23]. Mxene can be expressed by the chemical formula $M_{n+1}X_{n}T_{x}$ ($n=1\sim4$), where M is a transition metal element (T_{13} , T_{23} , T_{33} , T_{34} , T_{34} , T_{35} , T_{34} , where M is a surface functional group (-OH, -F, -O, etc.) [24,25].

However, the conductive transition metal core layer promotes high-speed electron transfer [24, 26]. The effectiveness of nZVI reduction will increase if coated with other nanoparticles, whereas, after coating, the tendency of nZVI and MXene composites prepared by reducing FeC1₂.4H₂O and synthesizing TiA1C₂ with LiF/HCl [27,28]. In addition, several factors can affect the adsorption process, such as adsorbent characteristics, solubility, and particle size [29,30]. In addition, environmental factors such as pH, temperature, and the length of contact time between the adsorbent and the adsorbate also affect the effectiveness of the adsorption results [31]. Under normal conditions or without treatment, CPFX has a pH range of 3.3-3.9. The difference in pH treatment in the study caused a shift in the maximum wavelength value (λ_{max}) of adsorption efficiency in CPFX. Previous studies have demonstrated the ability of nZVI-MXene nanocomposites to reduce metronidazole antibiotics, varying pH, adsorbate concentration, and temperature, without comparing them to the ability of pure nZVI and MXene [32]. These findings indicate that nZVI/MXene nanocomposites at 2:1 can effectively reduce CPFX and show advantages over previously studied materials. Therefore, this study was conducted to determine the characteristics of nZVI, MXene, and nZVI-MXene materials as adsorption media, to evaluate the effectiveness of nZVI, MXene, and nZVI-MXene nanoparticles in reducing CPFX concentration, and to assess the effect of pH and adsorption time on the CPFX reduction process.

2. Materials and Methods

2.1. Chemicals and materials.

The chemicals and materials used in this research include deionized water to make mixtures during the synthesis process and stabilize the pH. Ferrous sulfate heptahydrate (Fe₂SO₄.7H₂O) with a purity of 99.5% is the primary material used to make nZVI from Merck. Hydrochloric acid (HCl) makes hexa HF in MXene synthesis as a pH regulator. NH₄OH from Sigma-Aldrich, with a purity of 30-33%, is used to maintain the solution's stability by increasing pH. Sodium Borohydride (NaBH₄) is a reducing compound used to form nZVI. Ethanol, with a purity of 99.5%, cleans dirt and prevents rust on iron. Lithium Fluoride (LiF), with a purity of 98.5%, is used as an etching solution. Ti₃A1C₂, with a purity of 99%, is a basic material for making MXene. Cetyltrimethylammonium bromide (CTAB), with a purity of 98%, is a stabilizer during the formation of nanocomposites. Furthermore, ciprofloxacin creates target pollutants in adsorption experiments.

2.2. Preparation of nZVI nanoparticle synthesis.

The compound Fe₂SO₄.7H₂O 0.1 M weighed as much as 4.1703 g and was then dissolved into 150 mL of aqua bidest at 20-30°C in a glass beaker. Then, 3 g of CTAB (C₁₉H₄₂BrN) was added to 100 mL of aqua bidest. CTAB here functions as a surfactant to stabilize particles physically without chemical reactions. The two solutions were mixed and stirred using a magnetic stirrer, after which it was covered with parafilm. In another beaker, a 0.5 M NaBH₄ solution was prepared, and up to 1.892 g of NaBH₄ was dissolved in 100 mL of deionized water. Then, 5 mL of 25% NH4OH was added, and the solution was covered with parafilm. To reduce Fe³⁺ to Fe⁰, prepare a burette containing a NaBH4 solution at a rate of 10 mL/minute into the Fe2SO4.7H2O solution, with a total reaction time of 11 minutes and 30 seconds, and stir with a magnetic stirrer [33]. Later, the final color of the solution will be obtained, ranging from bluish-green to dark green and then to black. Furthermore, the solution is placed into a centrifuge tube and then centrifuged at 3000 rpm for 5 minutes at 25°C. The solution will separate from the iron powder, and the supernatant is discarded. This process is repeated three times using ethanol until nZVI is formed. As a post-treatment step, the final nZVI product was dried by placing it in a desiccator at room temperature to remove residual moisture and prevent oxidation or agglomeration, ensuring stability for further use.

2.3. Preparation of MXene nanoparticle synthesis.

The MXene synthesis process involves implementing in-situ HF etching using the LiF/HCl [28]. The HF etching process involves using hydrofluoric acid to remove material from a surface. This study was conducted by gradually adding the Ti₃A1C₂ compound to hydrochloric acid (HCl) and lithium fluoride (LiF) solutions. HCl was measured in a measuring cylinder to a volume of up to 31 mL, then diluted with deionized water until the final solution reached 40 mL, and then poured into an Erlenmeyer flask. 2 g of LiF was added to the Erlenmeyer flask and covered with aluminum foil. Furthermore, stirring was carried out with a magnetic stirrer for 20 minutes at room temperature to prepare the HCl/LiF etching solution.

$$LiF + HCl \rightarrow HF + LiCl$$
 (1)

$$Ti_3AlC_2 + 6HF \rightarrow Ti_3C_2F_3 + AlF_3 + 3H_2$$
 (2)

Furthermore, TiAlC₂ was added gradually into the Erlenmeyer flask and stirred at 35°C for 24-48 hours. The reaction was poured 10 mL into a centrifuge tube and centrifuged at 4000 rpm for 8 minutes at 25°C. Then, the supernatant solution was discarded, and the settled bottom layer was MXene. After the supernatant was discarded, 45 mL of aqua bidest was added to the tube and shaken quickly. Centrifugation was repeated 2-3 times until pH 6. After reaching that pH, the supernatant was discarded again, and then 20 mL of aqua bidest was added to each tube, shaken quickly by hand, and then poured into one sample bottle. Furthermore, ultrasonification was carried out for 1 hour using a probe ultrasonication operating at a frequency of 20 kHz and a power output of 200 W. The sample was kept on ice gel to maintain a cold temperature (~5-10°C) in the batch and preserve the solution's structure during ultrasonification. After that, the solution was divided back into four centrifuge tubes. Centrifugation was carried out at 4000 rpm for 8 minutes at 25°C. The supernatant was collected into a single container to obtain a MXene dispersion, specifically a single-layer MXene. However, there is still stratification in sedimentation. Water can be added to the final concentrate to dilute the dispersion. This solid solution is the MXene multilayer. To prevent agglomeration and ensure a more uniform dispersion of MXene, post-treatment drying was performed by placing the resulting material in a desiccator at room temperature. The gentle drying method helps to remove residual moisture without promoting restacking or structural collapse of the MXene layers, thus maintaining their dispersibility for further use.

2.4. Synthesis of nZVI-MXene nanocomposites.

Based on the results of previous studies on the removal of metamizole using nZVI/MXene, the ratios of nZVI-MXene nanocomposites used were 1:2, 1:1, and 3:1, respectively [28]. This study found that the % removal of the antibiotic metronidazole was higher at a ratio of 2:1. However, when the ratio of nZVI was increased again, the removal efficiency would decrease. From this, it was found that when the ratio between nZVI and MXene exceeded 2:1, it resulted in the aggregation of iron particles, which could inhibit electron transfer [28]. The comparison between nZVI and MXene composites was strengthened by the results of research conducted on the analysis of the physical properties of the ratios of N-Mxene-1, N-Mxene-2, and N-Mxene at ratios of 1:1, 1:2, and 2:1 [32]. The results obtained at a ratio of 2:1 had superior properties and surface area [28,32].

To synthesize nanocomposites, MXene is added to nZVI in a 2:1 ratio. Then, the mixture was placed in a centrifuge tube and centrifuged at 1000 rpm for 5 minutes at 25 °C. Furthermore, the solid will be separated from the solution. Washing is carried out with Aqua bidest. Then, it was filtered and rinsed with ethanol to prevent rusting reactions on iron and ensure the removal of impurities. As a final post-treatment step, the synthesized nZVI/MXene nanocomposite was dried in a desiccator at room temperature to eliminate residual moisture and maintain the material's stability.

2.5. Removal of ciprofloxacin.

CPFX solution was prepared by adding the required amount of drug into a 1 L beaker with the appropriate amount of deionized water. The degradation experiment was conducted in a batch form using a magnetic stirrer containing CPFX solutions with concentrations of 50, 100, and 200 mg/L. This study employed a concentration of 50 mg/L, as previous studies have detected CPFX content in pharmaceutical water ranging from 31 to 50 mg/L [10]. The use of

a concentration of 100 mg/L was based on a trial study examining CPFX content exposure to Daphnia magna for 48 hours, which showed that CPFX concentrations in the range of 0.01-100 mg/L had a toxic effect on the organisms. At the same time, using a concentration of 200 mg/L was intended to evaluate the effectiveness limit of the treatment method under extreme conditions and to test the maximum capacity of the treatment system before a decrease in efficiency occurred. The CPFX solution was adjusted to pH levels of 4, 7, and 9 by adding HCl or NaOH. The selection of pH in this study was intended to determine the removal efficiency results at acidic, neutral, and basic pH. The temperature used during the process is 25°C. After reaching the desired pH, the absorbent material is added to the beaker in an amount of up to 1.3 grams. Stirring is done during the reduction process at 200-300 rpm. After that, the solution is taken using a syringe filter at minutes 5, 10, 15, 20, 30, and 60, up to a volume of 5 mL. Then, the absorbance reading is performed on each solution using UV-vis spectrophotometry. A schematic diagram of the synthesis and experimental workflow is shown in Figure 1.

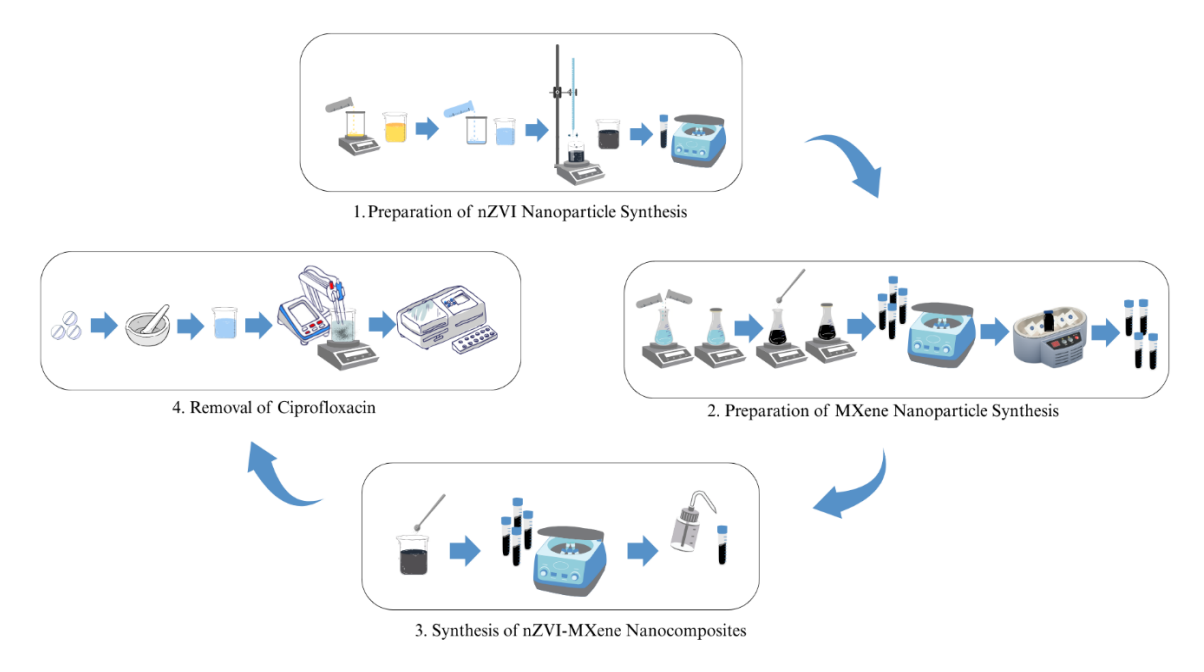


Figure 1. Schematic diagram of the synthesis and experimental workflow.

3. Results and Discussion

3.1. Materials characterization.

The shape of nZVI nanoparticles, based on the SEM results in Figure 2(a), shows that nZVI is round with an uneven surface. This is due to aggregation, a general characteristic of nZVI, which has high reactive properties and tends to clump to stabilize its surface energy. Meanwhile, in the MXene material, the SEM results in Figure 2(b) show a morphology with a layered structure. This can be interpreted as MXene having an interlayer between MXene layers, which expands the interlayer space of the material, as in Figure 2(c). According to previous studies, MXene can help prevent excessive nZVI aggregation by stabilizing through an enormous structure layer and surface area [32]. The morphology of the MXene interlayer space, which expands due to nZVI insertion, can be confirmed through BET analysis.

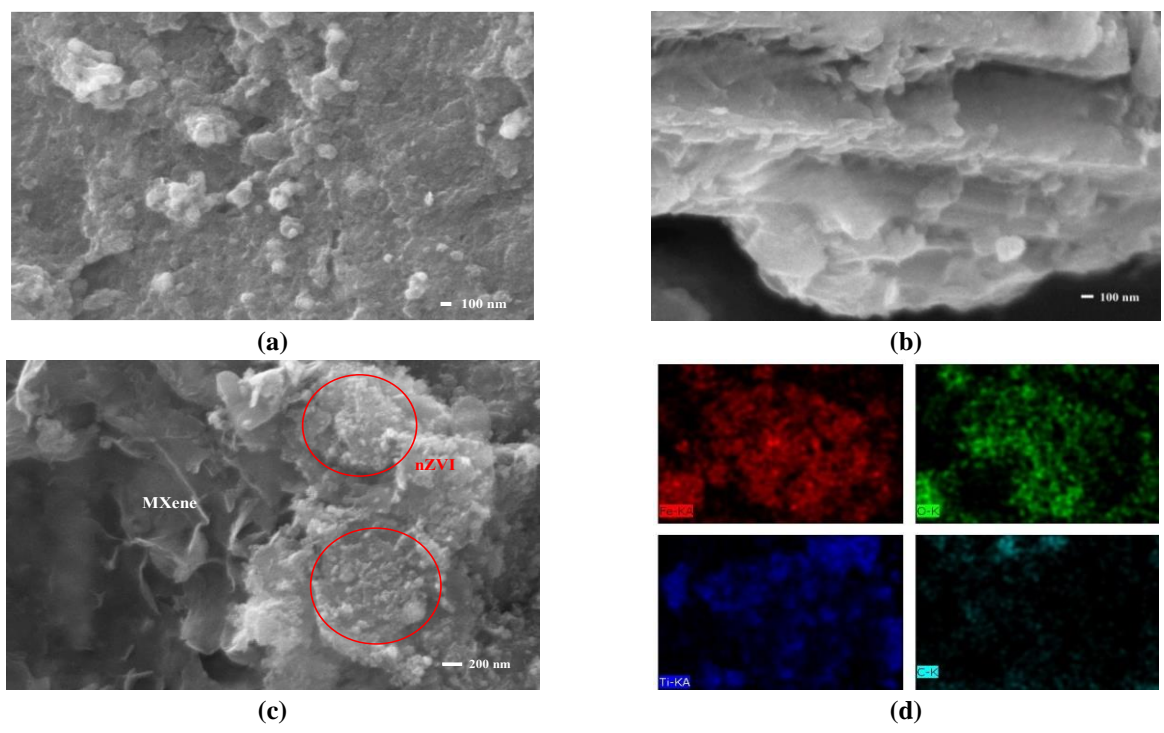


Figure 2. SEM image of: (a) nZVI; (b) MXene; (c) nZVI-MXene; (d) EDX of nZVI-MXene.

Based on the results of the material's physical properties in Table 2, there are significant differences in porosity and specific surface area (ET). nZVI particles have the highest BET surface area, 114.6 m²/g, indicating that nZVI particles have limited porosity and tend to aggregate [32, 33]. The pores in nZVI have a volume of 0.3 cm³/g with an average pore diameter of 11.8 nm, indicating that nZVI exhibits mesoporous characteristics (2-50 nm) [34, 35]. This study yields results that differ from those of previous studies, where the BET surface area of nZVI was reported to be 29.24 m²/g. [32]. This is due to differences in synthesis methods, preparation conditions, and characterization of the nZVI material used [36, 37]. In the study, the increase in the BET surface area of nZVI can be attributed to the use of CTAB surfactants, which prevent particle agglomeration and facilitate purification and washing, thereby ensuring stable particle morphology. Other factors, such as reduction method, precursor type, temperature, reaction time, and drying technique, can also affect the particle size, pore distribution, and specific surface area of nZVI [38,39]. In addition, the aggregation process of nZVI particles, which occurs due to the magnetic force between particles and high surface energy, can also cause significant variations in the BET surface area value [32].

Table 2. Physical characteristics of the material.

Materials	Adsorption average pore diameter (nm)	BET surface area (m²/g)	BJH Adsorption average pore radius (nm)	Pore volume (cm ³ /g)
nZVI	11.8	114.6	5.5	0.3
MXene	52.2	1.3	31.2	0.02
nZVI-MXene	20.6	1.5	9.1	0.01

Meanwhile, the MXene material has a much lower BET surface area of 1.3 m²/g, with an average pore diameter of 52.2 nm. This indicates that the MXene produced in this study exhibits macroporous characteristics (>50 nm) with a larger pore size than nZVI, but a smaller surface area [36]. In the nZVI-MXene composite, the BET surface area increased to 1.5 m²/g, which is higher than that of pure MXene. This indicates a bond between MXene and nZVI. In addition, the average pore diameter in the nZVI-MXene composite decreased to 20.6 nm, indicating that nZVI-MXene has mesoporous characteristics (2-50 nm), with a pore volume of

0.01 cm³/g [35]. This indicates that the insertion of nZVI particles into the MXene layer reduces the pore size and increases the relative surface area, as seen in the previous SEM results in Figure 1. Thus, although the BET surface area of the nZVI-MXene composite is not as high as that of pure nZVI, the insertion of nZVI into MXene produces a material with a smaller pore size and a more uniform distribution, thus improving the porosity characteristics of the material [35].

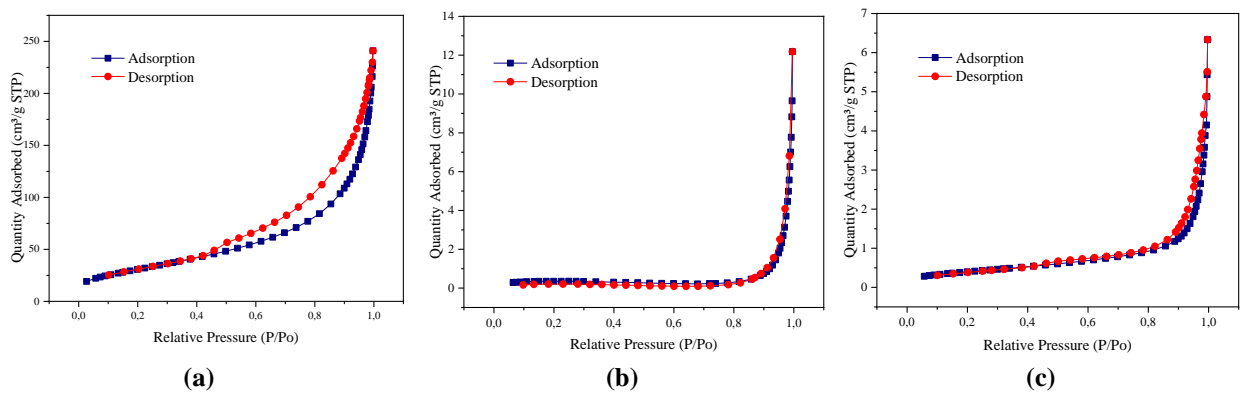


Figure 3. N₂ adsorption-desorption isothermal graph of: (a) nZVI; (b) MXene; (c) nZVI-MXene.

From Figure 3, the isothermal type can be analyzed based on the IUPAC classification with a graph showing the isothermal curves of Types II and IV. The Type II curve is the multilayer adsorption isothermal curve with the main characteristic describing physical adsorption on non-porous or mesoporous surfaces. It usually occurs in materials with large surface areas but low porosity. Meanwhile, the Type IV curve is commonly known as the mesoporous adsorption isothermal curve, with the main characteristic being adsorption on mesoporous materials, characterized by a hysteretic loop, which is a typical sign of capillary condensation. Based on the adsorption-desorption isothermal curve analysis in Figure 3(a), nZVI shows a significant increase in the amount of adsorbate at relatively high pressure (P/Po approaching 1) with a small H3-type hysteresis [34]. This pattern resembles the Type IV curve, typical for mesoporous materials (11.8 nm), indicating capillary adsorption in the mesoporous pores and lamellar structure with incompletely closed cracks. Although it has a high specific surface area (114.6 m²/g), the tendency of nZVI particle aggregation can reduce the effectiveness of adsorption. Meanwhile, the N₂ adsorption-desorption isothermal graph of the MXene material in Figure 3(b) exhibits the characteristics of a Type II curve according to the IUPAC classification [34]. The MXene curve exhibits a sharp increase at a relatively high P/Po pressure, approaching 1, but the amount of adsorbed adsorbate is significantly smaller than that of nZVI. This indicates that MXene is dominated by macropores, and the adsorption character is predominantly on the open surface with minimal pore contribution. The low specific surface area of MXene (1.3 m²/g) strengthens this property.

On the other hand, the nZVI-MXene in Figure 3(c) shows Type IV characteristics, with a significant increase at relatively high P/Po pressure and more pronounced H3-type hysteresis compared to nZVI [32]. The average pore size of 20.6 nm indicates mesoporous characteristics, where the combination of nZVI and MXene results in a more stable pore structure and a more even distribution of nZVI particles on the MXene surface. However, the specificity of nZVI-MXene allows for increased adsorption efficiency compared to both constituent materials [34].

The composition of nZVI, MXene, and nZVI-MXene materials is shown in Table 3. The nZVI-MXene nanocomposite has a carbon (C) value of 6,76% less than pure nZVI and MXene, which have C values of 12.47% and 31.08%, respectively (Table 3). This finding

aligns with previous studies, which acknowledge that carbon is necessary for synthesizing nZVI and is not an intentional aspect [32]. Several factors contribute to the carbon content in nZVI, one of which is the synthesis process and the use of ethanol with a purity of 99.5% to purify the final product. Ethanol is an organic solvent containing elements C, H, and O. This can cause the appearance of carbon attached to the surface of nZVI [32]. However, the content of the Oxygen (O) element in the nZVI-MXene nanocomposite is smaller than that of pure nZVI. This contradicts previous research, which found that nZVI-MXene had the highest oxygen content.

Table 3. The elemental composition of the materials was obtained through EDX mapping.

Materials	C (%)	O (%)	Ti (%)	Fe (%)
nZVI	12.47	38.48	-	49.05
MXene	31.08	23.76	45.16	-
nZVI-MXene	6.76	32.71	30.28	30.24

The imperfect formation of a new functional group containing oxygen in nZVI-MXene could cause this. The imperfect formation of new oxygen-containing functional groups in nZVI-MXene can cause this. For example, during the synthesis process, oxide groups form on the surface of nZVI, which is more susceptible to oxidation by dissolved oxygen or water, resulting in oxide layers such as FeO, Fe₂O₃, or Fe₃O₄ on its surface. The quantity of Fe in nZVI-MXene (30.24%) is smaller than that of pure nZVI (49.05%). This also occurs in the Ti element, the main element forming MXene, where the Ti content value drops to 15% from pure MXene. The distribution of elements in the nZVI-MXene nanocomposite is shown in Figure 1(d). These results show that the elements O, Ti, and Fe in the nanocomposite have an even distribution. This contrasts with element C, which is only found at a few points.

The -OH group was detected at an absorption band of 3675 cm-1 on the nZVI-MXene composite. In MXene, the -OH group was found at 3652 cm⁻¹ (Table 4). The presence of the -OH group can increase the hydrophilicity of the nZVI and MXene surface to facilitate the diffusion of water molecules and dissolved pollutants to the material's surface. This is important to ensure that a pollutant can easily reach the active site on the material's surface. The Fe-O bond was detected on the MXene surface with a value of 648 cm⁻¹ after adding nZVI during the synthesis of the composite. The presence of the Fe-O bond on the nZVI-MXene surface indicates the presence of an iron oxide phase that has catalytic properties and can produce free radicals in an aqueous environment that functions to degrade organic pollutants. At the peak of the 670 cm⁻¹ absorption band, the Fe-O and Ti-O bonds are stretched. According to previous studies, the absorption band range of FeOOH [32]. The nanocomposite surface shown in Figure 4 indicates the successful synthesis, with the definite Fe content and the presence of significant hydroxyl and oxygen groups [32].

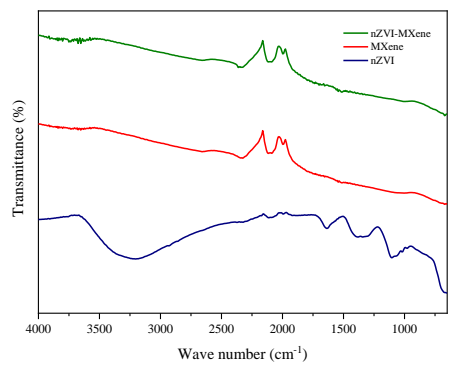


Figure 4. FTIR image of nZVI, MXene, and nZVI-MXene.

Table 4. Summary of each characterization method.								
Characterization method	nZVI	MXene	nZVI-MXene					
SEM	round with an uneven surface	show a morphology with a layered structure	interlayer structure, which expands the interlayer space of the material					
EDX	C (12.47%), O (38.48%), Fe (49.05%)	C (31.08%), O (23.76%), Ti (45.16%)	C (6.76%), O (32.71%), Ti (30.28%), Fe (30.24%)					
Isothermal type	Type IV curve with a small H3 type hysteresis is commonly known as the mesoporous adsorption isothermal curve	Type II curve is the multilayer adsorption isothermal curve	Type IV curve with more pronounced H3-type hysteresis is commonly known as the mesoporous adsorption isothermal curve					
FTIR	Fe-O bonds were detected on the nZVI surface with a value of 670 cm ⁻¹	-OH group was found at 3652 cm ⁻¹	-OH group was detected at the absorption band of 3675 cm ⁻¹ , Fe-O bond was detected on the MXene surface with a value of 648 cm ⁻¹					

Table 4. Summary of each characterization method

3.2. Analysis of the effect of concentration variation, pH, and CPFX contact time.

In this study, concentration variations were conducted to determine the optimal concentration at which the adsorbent can effectively reduce CPFX. The graph in Figure 5 shows that each material has a different optimum adsorption capacity at pH 7.

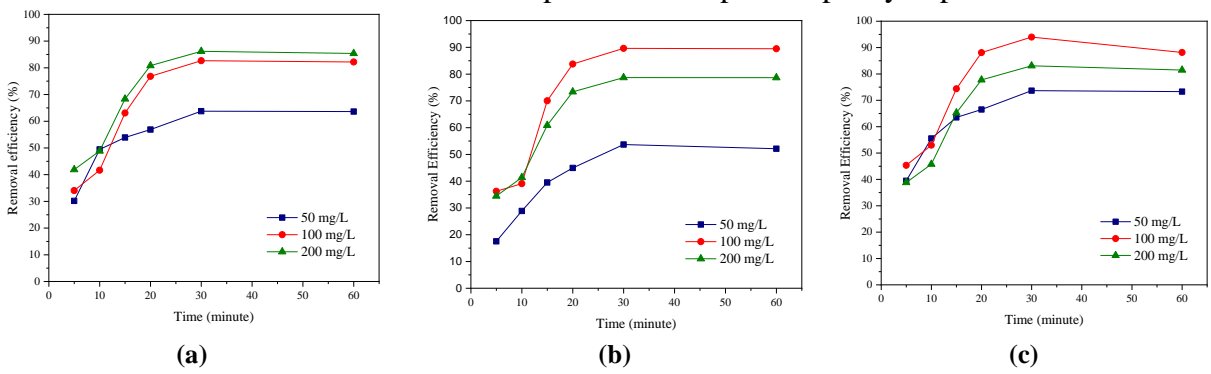


Figure 5. Adsorbate removal efficiency at each solution concentration (a) nZVI; (b) MXene; (c) nZVI-MXene.

NZVI nanoparticles have a removal efficiency of 86.17% against a CPFX solution with a concentration of 200 mg/L. It can also be seen in Figure 5(a) that in nZVI, the increase in solution concentration is directly proportional to the rise in removal efficiency. This differs from MXene and nZVI-MXene nanocomposites, which exhibit optimal removal efficiency against the CPFX solution at a concentration of 100 mg/L, with values of 89.62% and 89.62%, respectively. It can be seen in Figure 5(b)-(c) that when at a concentration of 200 mL or, in other words, exceeding 100 mg/L, the removal efficiency of the material will decrease by 11%. In previous studies on metradizole removal using nZVI-MXene, the removal efficiency of the material decreased as the solution concentration increased. In addition, other studies on naphthalene removal using nZVI-MXene have shown that the removal efficiency of the material decreases relatively from a concentration of 100 mg/L to 500 mg/L. Therefore, in this study, the optimum concentration of material removal using nZVI-MXene was 100 mg/L and decreased significantly at higher concentrations.

At pH variation, sample analysis was performed on each material with a 100 mg/L concentration. The graph in Figure 6 shows that each material has a CPFX removal efficiency of 100 mg/L at pH 9. This follows previous research on CPFX removal using LaFeO₃/polystyrene, which has the highest CPFX removal efficiency at pH 9 [41]. nZVI,

MXene, and nZVI-MXene materials have hydroxyl (-OH) or oxide groups on their surfaces, as evidenced by previous FTIR analysis. This means that the charge in the material changes rapidly depending on the pH of the solution. At a pH of 9, the surface of the adsorbent tends to be negatively charged due to the ionization of the hydroxyl groups. Under these conditions, the amphoteric CPFX molecules are positively charged, which causes electrostatic interactions between the adsorbent and the CPFX surface [28]. According to previous research, at higher pH, H⁺ ions will be in solution rather than on the material's surface, so that the material's surface will be negatively charged. According to previous studies, the amphoteric nature of CPFX is attributed to the presence of amine groups (-NH2) that can accept protons, thereby acting as bases, and carboxylate groups (-COOH) that can transfer protons, thereby acting as acids [12]. Other studies also mention that at pH 5 and 7, CPFX has a weak cation charge [41]. In contrast, at pH 9, CPFX is more susceptible to attack by active species than cationic forms due to the higher electron density in the neutral form, which is more hydrophobic than cations. Therefore, the removal efficiency of CPFX is higher at pH 9.

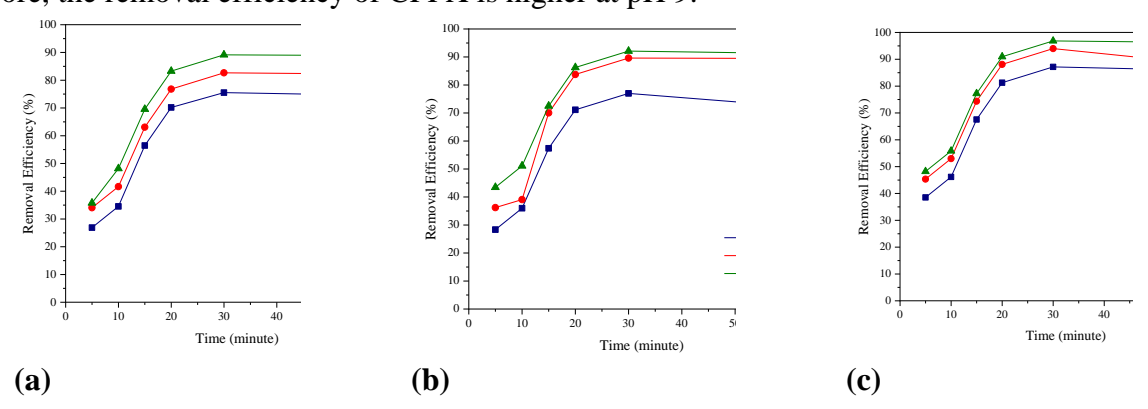


Figure 6. Adsorbate removal efficiency at each pH variation of the solution (a) nZVI; (b) MXene; (c) nZVI-MXene.

Then, an analysis of the material's effectiveness was carried out using a CPFX concentration of 100 mg/L and a pH of 9, as shown in Figure 7. It was found that under these conditions, the nZVI-MXene nanocomposite had a higher removal efficiency of 96.82%. For nZVI and MXene, respectively, it was 89.15% and 92.1%. This also strengthens the evidence for the morphological characteristics of each material, highlighting the superiority of the nZVI-MXene nanocomposite over other materials.

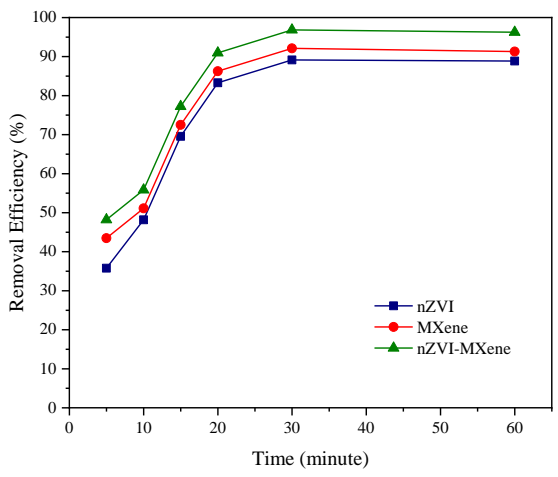


Figure 7. Effect of CPFX contact time.

In the variation of the contact time, namely at 5, 10, 15, 20, 30, and 60 minutes, it can be concluded from Figure 6 that each material exhibits a significant efficiency increase within the 5-20 minute time range. However, when the contact time ranges from 20 to 30 minutes, there is only a slight increase, and it tends to decrease at a contact time of 60 minutes. This is because the adsorption capacity generally increases gradually until it reaches equilibrium. At the beginning of the adsorption process, the surface of the adsorbent is still not much bound to CPFX, so the tendency of the solution absorbed by the adsorbent can be higher. When the surface of the absorbent reaches the equilibrium point, it will experience saturation and will no longer be able to absorb more CPFX. From these data, the optimum time for CPFX adsorption is 30 minutes. This is in line with previous research, which states that the equilibrium point occurs at 30-60 minutes, as the number of remaining active sites decreases after this time, making it difficult for CPFX molecules that have not been adsorbed to find a binding site on the adsorbent surface [28].

Although nZVI has the highest BET surface area (114.6 m²/g) compared to MXene (1.3 m²/g) and nZVI-MXene (1.5 m²/g), the best removal efficiency was shown by nZVI-MXene. This proves that surface area is not the only factor determining adoption efficiency [37]. The higher efficiency of nZVI-MXene may be attributed to the synergistic interaction between nZVI and MXene, where nZVI provides high reactivity, while MXene enhances the stability of the material [32]. The mechanism of this interaction is shown by nZVI releasing electrons during Fe oxidation. With the help of MXene, these electrons break down dissolved O₂ to form reactive radicals such as hydroxyl radical (•OH) and superoxide radicals (O₂••), which have strong oxidative content for CPFX degradation [12]. In addition, the surface chemistry of nZVI-MXene allows more effective electrostatic interaction, especially at pH 9, where the surface changes of the adsorbent and adsorbate interact optimally. The more even distribution of active sites in the composite structure also maximizes the adsorption of CPFX, making the adsorption process more efficient.

Therefore, in this experiment, the quality of chemical interaction and material morphology has a more significant effect on adsorption efficiency than specific surface area [36]. In this study, the removal of CPFX using nZVI-MXene was considered better, with the highest removal efficiency of 96.82%. In previous studies, the photolytic process using TiO₂-NTA to remove ciprofloxacin antibiotics in WWTP achieved a removal efficiency of 53-69%, whereas photocatalytic oxidation could reach 93-100% [40]. In other studies, the removal of CPFX using a pure LFO photo-fenton system was 54%, and LFO/PS was 79.88% [40]. In this study, the most optimal photocatalytic method was achieved through photocatalytic oxidation using TiO2-NTA, resulting in a CPFX removal efficiency of 100%. MXene, with its high conductivity and active functional groups such as -OH and Ti-O, can facilitate efficient electron transfer. In contrast, nZVI exhibits a high reduction ability, producing reactive radicals (•OH). This combination creates a synergy between adsorption, reduction, and oxidative degradation, which is enhanced by UV or visible light irradiation [28]. Based on several studies, it is suggested that further research incorporate a photocatalytic process into the CPFX removal process using nZVI-MXene nanocomposite to enhance its efficiency. Increasing efficiency using photocatalysts can permanently degrade contaminants, utilize light as an energy source, and achieve higher efficiency while maintaining a sustainable process. By optimizing parameters such as concentration, light source, and reaction conditions, integrating nZVI-MXene with the photocatalytic oxidation process can be an effective solution for CPFX treatment. Moreover, future research should also focus on how these promising laboratoryscale results can be translated into actual WWTP applications by evaluating their scalability, operational stability, cost-effectiveness, and integration with existing wastewater treatment systems.

4. Conclusions

Synthesis of nZVI-MXene monocomposite resulted in morphological changes in the material compared to pure nZVI and MXene. In nZVI nanoparticles, the specific surface area is 114.6 m²/g, and the pore diameter is 11.8 nm, which indicates limited porosity and a tendency to aggregate. Meanwhile, MXene has a specific surface area value of 1.26 m²/g and a pore diameter of 52.2 nm. In the nZVI-MXene nanocomposite, the specific surface area increases to 1.47 m²/g, and the pore diameter is smaller at 20.6 nm. This indicates a bond between MXene and nZVI. nZVI nanoparticles exhibit optimal removal efficiency at CPFX with a concentration of 200 mg/L, achieving 86% removal efficiency. In contrast to MXene and nZVI-MXene, which exhibit optimal removal efficiencies against the CPFX solution at a concentration of 100 mg/L, with values of 89.6% and 94%, respectively, the removal efficiency of the material decreases by 11% when the CPFX concentration exceeds 100 mg/L. nZVI, MXene, and nZVI-MXene materials exhibit optimal removal efficiencies against 100 mg/L CPFX at pH 9, with values of 89%, 92%, and 97%, respectively. The optimum contact time for CPFX adsorption is 30 minutes. Although nZVI has the highest BET surface area compared to MXene and nZVI-MXene, nZVI-MXene has the best removal efficiency. This demonstrates that surface area is not the sole factor determining adsorption efficiency. Thus, in this experiment, the quality of chemical interaction and the morphology of the materials have a more significant influence on the adsorption efficiency than just the specific surface area.

Author Contributions

Conceptualization, I.I.F., A.Y.; methodology, I.I.F., E.N.; validation, A.Y., A.P.; formal analysis, I.I.F.; investigation, E.N., A.P.; resources, A.Y.; data curation, I.I.F.; writing—original draft preparation, I.I.F.; writing—review and editing, A.Y., E.N.; visualization, A.P.; supervision, A.Y.; project administration, A.Y.; funding acquisition, A.Y. All authors have read and agreed to the published version of the manuscript.

Institutional Review Board Statement

Not applicable.

Informed Consent Statement

Not applicable.

Data Availability Statement

The data presented in this study are available on request from the corresponding author.

Funding

Research funded by Institut Teknologi Sepuluh Nopember (1207/PKS/ITS/2024).

Acknowledgments

Thanks to the Directorate of Research and Community Service of the Sepuluh Nopember Institute of Technology and the Ministry of Education, Culture, Research, and Technology for supporting this research through the Fundamental Research Fund for Year 2024.

Conflicts of Interest

The authors declare that they have no financial conflicts or personal relationships that could have influenced the work reported in this paper.

References

- 1. Wang, L.; Xu, Y.; Qin, T.; Wu, M.; Chen, Z.; Zhang, Y.; Liu, W.; Xie, X. Global trends in the research and development of medical/pharmaceutical wastewater treatment over the half-century. *Chemosphere* **2023**, *331*, 138775, https://doi.org/10.1016/j.chemosphere.2023.138775.
- 2. Tehrani, E.; Faraji, A.R.; Shojaei, N.; Shahinmehr, S.; Najafi, A.; Hekmatian, Z.; Tehrani, Z.; Bornas, B. An overview of the characteristics, toxicity, and treatment methods for the degradation of pharmaceutically active compounds: Naproxen as a case studyJ. Environ. Chem. Eng. **2023**, *11*, 111575, https://doi.org/10.1016/j.jece.2023.111575.
- 3. Kumar, V.; Lakkaboyana, S.K.; Sharma, N.; Chakraborty, P.; Umesh, M.; Pasrija, R.; Thomas, J.; Kalebar, V.U.; Jayaraj, I.; Awasthi, M.K.; Das, T.; Oladipo, A.A.; Barcelo, D.; Dumee, L.F. A critical assessment of technical advances in pharmaceutical removal from wastewater A critical review. *Case Stud. Chem. Environ. Eng.* **2023**, *8*, 100363, https://doi.org/10.1016/j.cscee.2023.100363.
- Mojoyinola, A.O.; Ishaya, H.B.; Makena, W.; Jacob, C.B.; Jonga, U.M.; Anochie, V.C.; Denis, E.W.; Gadzama, M.N. Protective effect of ciprofloxacin-induced oxidative stress, testicular and hepatorenal injury by *Citrullus lanatus* L. (Watermelon) seeds in adult Wistar rats. *S. Afr. J. Bot.* 2023, 156, 365-375, https://doi.org/10.1016/j.sajb.2023.03.017.
- 5. Qalyoubi, L.; Al-Othman, A.; Al-Asheh, S. Removal of ciprofloxacin antibiotic pollutants from wastewater using nano-composite adsorptive membranes. *Environ. Res.* **2022**, *215*, 114182, https://doi.org/10.1016/j.envres.2022.114182.
- Kose-Mutlu, B.; Ilyasoglu, G.; Ardic, R.; Ahmet Demirbilekli, M.; Koyuncu, I. Removal of emerging organic micropollutants from real hospital wastewater by modified ultrafiltration membranes. *Sep. Purif. Technol.* 2025, 357, 129960, https://doi.org/10.1016/j.seppur.2024.129960.
- 7. Souza, H.d.O.; Costa, R.d.S.; Quadra, G.R.; Fernandez, M.A.d.S. Pharmaceutical pollution and sustainable development goals: Going the right way?. *Sustain. Chem. Pharm.* **2021**, *21*, 100428, https://doi.org/10.1016/j.scp.2021.100428.
- 8. Khan, P.; Saha, R.; Halder, G. Towards sorptive eradication of pharmaceutical micro-pollutant ciprofloxacin from aquatic environment: A comprehensive review. *Sci. Total Environ.* **2024**, *919*, 170723, https://doi.org/10.1016/j.scitotenv.2024.170723.
- 9. Yisa, A.G.; Chia, M.A.; Gadzama, I.M.K.; Oniye, S.J.; Sha'aba, R.I.; Gauje, B. Immobilization, oxidative stress and antioxidant response of *Daphnia magna* to Amoxicillin and Ciprofloxacin. *Environ. Toxicol. Pharmacol.* **2023**, *98*, 104078, https://doi.org/10.1016/j.etap.2023.104078.
- 10. Sathishkumar, K.; Naraginti, S.; Lavanya, K.; Zhang, F.; Ayyamperumal, R.; Liu, X. Intimate coupling of gC₃N₄/CdS semiconductor on eco-friendly biocarrier loofah sponge for enhanced detoxification of ciprofloxacin. *Environ. Res.* **2023**, *235*, 116558, https://doi.org/10.1016/j.envres.2023.116558.
- 11. Rosas-Ramírez, J.R.; Orozco-Hernández, J.M.; Elizalde-Velázquez, G.A.; Raldúa, D.; Islas-Flores, H.; Gómez-Oliván, L.M. Teratogenic effects induced by paracetamol, ciprofloxacin, and their mixture on *Danio rerio* embryos: Oxidative stress implications. *Sci. Total Environ.* **2022**, *806*, 150541, https://doi.org/10.1016/j.scitotenv.2021.150541.
- 12. Ricky, R.; Shanthakumar, S. Removal of ciprofloxacin from aqueous media by *Chlorella pyrenoidosa*, *Scenedesmus obliquus*, and isolated *Stichococcus bacillaris*: A comparative study on toxicity, removal mechanism and biochemical composition. *J. Environ. Chem. Eng.* **2023**, *11*, 109990, https://doi.org/10.1016/j.jece.2023.109990.
- 13. Huong, V.H.; Nguyen, V.-C.; Pham, K.-P.; Nguyen, T.B.; Ngac, A.B.; Thi Loan, T. Construction dual active https://biointerfaceresearch.com/

- sites on SnO₂ via Fe doping for effective ciprofloxacin photodegradation. *J. Alloys Compd.* **2024**, *1005*, 176020, https://doi.org/10.1016/j.jallcom.2024.176020.
- 14. Eltaweil, A.S.; Ahmed, M.S.; El-Subruiti, G.M.; Khalifa, R.E.; Omer, A.M. Efficient loading and delivery of ciprofloxacin by smart alginate/carboxylated graphene oxide/aminated chitosan composite microbeads: *In vitro* release and kinetic studies. *Arab. J. Chem.* **2023**, *16*, 104533, https://doi.org/10.1016/j.arabjc.2022.104533.
- 15. Mohammed, N.A.H.; Shamma, R.N.; Elagroudy, S.; Adewuyi, A. Copper ferrite immobilized on chitosan: A suitable photocatalyst for the removal of ciprofloxacin, ampicillin and erythromycin in aqueous solution. *Catal. Commun.* **2023**, *182*, 106745, https://doi.org/10.1016/j.catcom.2023.106745.
- González-Ballesteros, N.; Martins, P.M.; Tavares, C.J.; Lanceros-Méndez, S. Quercetin-mediated green synthesis of Au/TiO₂ nanocomposites for the photocatalytic degradation of antibiotic ciprofloxacin. *J. Ind. Eng. Chem.* 2025, 143, 526-537, https://doi.org/10.1016/j.jiec.2024.09.003.
- 17. Shanableh, A.; Bhattacharjee, S.; Sadik, S. Evaluating iron-based nanoparticles for ciprofloxacin removal: Date seed extract as a biostabilizing and a bioreducing agent. *J. Water Process Eng.* **2021**, *44*, 102419, https://doi.org/10.1016/j.jwpe.2021.102419.
- 18. Ali, Z.T.A.; Abdulhusain, N.A. Containment of ciprofloxacin and copper in groundwater using nanocomposite prepared by the use of pomegranate peel extract: characterization, kinetic, and modeling study. *Desalin. Water Treat.* **2023**, *315*, 327–341, https://doi.org/10.5004/dwt.2023.30139.
- Banda, P.G.; Kurup, G.B.; Mucherla, R. Immobilization of Ag nanoparticles on NiFe₂O₄@TiO₂@PDA: Multifunctional catalytic action toward the reduction of 4-Nitrophenol and photodegradation of methylene blue and ciprofloxacin. *J. Phys. Chem. Solids* 2023, 181, 111556, https://doi.org/10.1016/j.jpcs.2023.111556.
- 20. Krithika Shree, S.; Namasivayam, S.K.R.; Pandian, A. Sustainable developmental measures for the treatment of pharmaceutical industry effluent using nano zero valent iron technology (nZVI) A review. *J. Water Process Eng.* **2023**, *56*, 104390, https://doi.org/10.1016/j.jwpe.2023.104390.
- 21. Thakur, A.; Kumar, A.; Singh, A. Adsorptive removal of heavy metals, dyes, and pharmaceuticals: Carbon-based nanomaterials in focus. *Carbon* **2024**, *217*, 118621, https://doi.org/10.1016/j.carbon.2023.118621.
- 22. Zhou, Y.; Leong, S.Y.; Li, Q. Modified biochar for removal of antibiotics and antibiotic resistance genes in the aqueous environment: A review. *J. Water Process Eng.* **2023**, 55, 104222, https://doi.org/10.1016/j.jwpe.2023.104222.
- 23. Li, R.; Sun, F.; Liu, Z.; Shi, Y.; He, S.; Chen, J. Research progress and prospect of covalent organic frameworks (COFs) and composites: From synthesis to application in water contaminants. *J. Environ. Chem. Eng.* **2024**, *12*, 113944, https://doi.org/10.1016/j.jece.2024.113944.
- 24. Qin, M.; Merzougui, C.; Su, Y.-m.; Li, Y.-f.; Chen, W.-y.; Huang, D. Recent developments in MXene and MXene/carbon composites for use in biomedical applications. *New Carbon Mater.* **2023**, *38*, 496-506, https://doi.org/10.1016/S1872-5805(23)60730-9.
- 25. Zu, P.; Xing, X.; Wan, H.; Yan, G.; Zhang, G. Preparation of larger MXene layers and research progress in the field of gas adsorption and separation. *Sep. Purif. Technol.* **2023**, *327*, 125010, https://doi.org/10.1016/j.seppur.2023.125010.
- 26. Xue, W.; Shi, X.; Guo, J.; Wen, S.; Lin, W.; He, Q.; Gao, Y.; Wang, R.; Xu, Y. Affecting factors and mechanism of removing antibiotics and antibiotic resistance genes by nano zero-valent iron (nZVI) and modified nZVI: A critical review. Water Res. 2024, 253, 121309, https://doi.org/10.1016/j.watres.2024.121309.
- 27. Chi, H.-Y.; Zhou, X.-X.; Wu, M.-R.; Shan, W.-y.; Liu, J.-f.; Wan, J.-q.; Yan, B.; Liu, R. Regulating the reaction pathway of nZVI to improve the decontamination performance through magnetic spatial confinement effect. *J. Hazard. Mater.* **2023**, 447, 130799, https://doi.org/10.1016/j.jhazmat.2023.130799.
- 28. Chen, C.; Luo, W.; Xu, J.; Niu, D. Investigation of the adsorption and degradation of metronidazole residues in agricultural wastewater by nanocomposite based on nZVI on MXene. *Alex. Eng. J.* **2023**, *80*, 41–47, https://doi.org/10.1016/j.aej.2023.08.055.
- 29. Hussain, N.; Khan, H.; Hussain, S.; Arshad, M.; Umar, M.; Wahab, F. Unleashing the dye adsorption potential of polyaminoimide homopolymer: DFT, statistical physics, site energy and pore size distribution analyses. *J. Environ. Chem. Eng.* **2023**, *11*, 111383, https://doi.org/10.1016/j.jece.2023.111383.
- Zakirov, T.R.; Mikhailova, A.N.; Varfolomeev, M.A.; Yuan, C. Pore-scale study of dynamic adsorption of a water-soluble catalyst during drainage displacement in porous media using lattice Boltzmann simulations. *International Int. Commun. Heat Mass Transf.* 2023, 145, 106810,

- https://doi.org/10.1016/j.icheatmasstransfer.2023.106810.
- 31. Bayuo, J.; Rwiza, M.J.; Choi, J.W.; Mtei, K.M.; Hosseini-Bandegharaei, A.; Sillanpää, M. Adsorption and desorption processes of toxic heavy metals, regeneration and reusability of spent adsorbents: Economic and environmental sustainability approach. *Adv. Colloid Interface Sci.* **2024**, *329*, 103196, https://doi.org/10.1016/j.cis.2024.103196.
- 32. Raza Ul Mustafa, M.; Khurshid, H.; Isa, M.H. Nanoscale zero-valent iron (NZVI) intercalated MXene (Ti₃C₂T_x) for removal of polycyclic aromatic hydrocarbons in wastewater. *J. Environ. Chem. Eng.* **2024**, *12*, 112149, https://doi.org/10.1016/j.jece.2024.112149.
- 33. Li, Y.; Zhou, S.; Meng, Y.; Qiu, Y.; Chen, M.; Ma, L.; Li, L.; Liu, Y.; Yang, B. Advances in modified zero-valent iron materials: Synthesis methods, field studies, practical applications and challenges. *Chem. Eng. J.* **2024**, *502*, 157832, https://doi.org/10.1016/j.cej.2024.157832.
- 34. Muttakin, M.; Mitra, S.; Thu, K.; Ito, K.; Saha, B.B. Theoretical framework to evaluate minimum desorption temperature for IUPAC classified adsorption isotherms. *Int. J. Heat Mass Transf.* **2018**, *122*, 795–805, https://doi.org/10.1016/j.ijheatmasstransfer.2018.01.107.
- 35. Qiang, H.; Shi, M.; Lu, K.; Wang, F.; Xia, M. Green self-templated synthesis of P-doped mesoporous carbon from dual sodium salts with improved average pore size for capacitive deionization. *Desalination* **2025**, *593*, 118246, https://doi.org/10.1016/j.desal.2024.118246.
- 36. Gao, T.; Li, H.; Zhou, F.; Gao, M.; Liang, S.; Luo, M. Mesoporous carbon derived from ZIF-8 for high efficient electrosorption. *Desalination* **2019**, *451*, 133–138, https://doi.org/10.1016/j.desal.2017.06.021.
- 37. Jia, Y.; Hu, X.; Huang, H.; Deng, Y.; Cao, W.; Zhou, Y.; Hou, X. Pore structure regulation of nano-CdSnO₃ based on particles adhesion and mass transfer for enhanced NO-sensing. *Sens. Actuators B: Chem.* **2025**, 422, 136624, https://doi.org/10.1016/j.snb.2024.136624.
- 38. Muñoz, H.J.; Korili, S.A.; Gil, A. Surface tuning of a highly crystalline Ni/LaAlO₃ perovskite catalyst obtained from aluminum saline slags using various synthesis methods for the dry reforming of methane. *Catal. Today* **2025**, *447*, 115158, https://doi.org/10.1016/j.cattod.2024.115158.
- 39. You, N.; Chen, Z.; Gao, Z.; Song, X. The effect of copper slag as a precursor on the mechanical properties , shrinkage and pore structure of alkali-activated slag-copper slag mortar. *J. Build. Eng.* **2024**, *98*, 111151, https://doi.org/10.1016/j.jobe.2024.111151.
- 40. Abromaitis, V.; Oghenetejiro, O.A.M.A.; Sulciute, A.; Urniezaite, I.; Sinkeviciute, D.; Zmuidzinaviciene, N.; Jankunaite, D.; Dzingeleviciene, R.; Baranauskis, K.; Martuzevicius, D. TiO₂ nanotube arrays photocatalytic ozonation for the removal of antibiotic ciprofloxacin from the effluent of a domestic wastewater treatment plant: Towards the process upscaling. *J. Water Process Eng.* 2024, 63, 105457, https://doi.org/10.1016/j.jwpe.2024.105457.

Publisher's Note & Disclaimer

The statements, opinions, and data presented in this publication are solely those of the individual author(s) and contributor(s) and do not necessarily reflect the views of the publisher and/or the editor(s). The publisher and/or the editor(s) disclaim any responsibility for the accuracy, completeness, or reliability of the content. Neither the publisher nor the editor(s) assume any legal liability for any errors, omissions, or consequences arising from the use of the information presented in this publication. Furthermore, the publisher and/or the editor(s) disclaim any liability for any injury, damage, or loss to persons or property that may result from the use of any ideas, methods, instructions, or products mentioned in the content. Readers are encouraged to independently verify any information before relying on it, and the publisher assumes no responsibility for any consequences arising from the use of materials contained in this publication.